Experimental crystallization of gallium: ultrasonic measurements of elastic anisotropy and implications for the inner core

Daniel Brito [a,b,*], David Elbert [b], Peter Olson [b]

[a] *LGIT, Observatoire de Grenoble, Grenoble, France*
[b] *Department of Earth and Planetary Sciences, Johns Hopkins University, Baltimore, MD, USA*

Abstract

We present ultrasonic measurements of elastic anisotropy in gallium undergoing directional solidification in the presence of imposed thermal gradients, rotation, convection, turbulence, and magnetic fields. Simultaneous in situ measurements of temperature and compressional wave speed are used to track the crystallization front during solidification. We find that individual solidified gallium samples are always polycrystalline and elastically anisotropic, with grains elongated in the solidification direction. The measured compressional wave anisotropy in individual solid samples ranges from 20 to 80% of the single crystal values, depending on experimental conditions. We also find the amount of elastic anisotropy varies with position in an individual sample. Based on ensemble averages from multiple experiments made under similar environmental conditions, we find the direction of elastic anisotropy in the solid is sensitive to the thermal gradient direction, while the amount of anisotropy is most sensitive to the presence or absence of initial nucleation in the melt. Experiments that show average anisotropy have the ultrasonically fast axis aligned with gravity and the thermal gradient. Strongly anisotropic solids result when nucleation grains are present in the initial melt, whereas smaller or zero average anisotropy results when nucleation grains are initially absent. Other externally imposed factors we have examined, such as turbulence and magnetic fields, have either no measurable influence or tend to reduce the amount of anisotropy of the solid. Our results suggest that during crystallization of Earth's inner core, the orientation of average anisotropy in the newly formed solid is controlled primarily by radial solidification, while the amount of anisotropy may be influenced by pre-existing inner core texture. © 2002 Elsevier Science B.V. All rights reserved.

1. Introduction

Numerous seismic investigations have concluded that the Earth's solid inner core has a large-scale anisotropy. The fundamental observation, first reported by Poupinet et al. (1983), is that seismic compressional waves travel faster through the inner core along polar paths than along equatorial paths. These directional differences in wave speed are usually attributed to elastic anisotropy, resulting from preferred crystal alignment that is coherent on a large scale. Early investigations concluded the seismic anisotropy is axisymmetric to first-order, with a compressional wave speed 3% greater along the pole than the equator (see Morelli et al., 1986). As additional observations have become available, however, this simple picture has been replaced by an increasingly complex one (see Song, 1997). Now there is evidence for heterogeneity in anisotropy on spatial scales as small as 10 km (Vidale and Earle, 2000), and also evidence that anisotropy is absent in the outermost portion

* Corresponding author..
E-mail address: Daniel.Brito@ujf-grenoble.fr (D. Brito).

of the inner core (McSweeney et al., 1997; Song and Helmberger, 1998). Perhaps most puzzling, the western hemisphere of the inner core appears more anisotropic than the eastern hemisphere (Tanaka and Hamaguchi, 1997; Creager, 1999). Departures from axial symmetry in the anisotropy are significant for several reasons. First, they indicate that effects other than Earth's rotation govern the gross structure of the inner core. Second, the non-axial structure provides a mean for seismic detection of possible anomalous rotation of the inner core (Song and Richards, 1996; Creager, 1997; Laske and Masters, 1999; Souriau and Poupinet, 2000).

Although most interpretations of the inner core seismic anisotropy presume it is a consequence of preferred crystal alignment, there is no consensus on the origin of alignment, or what factors exert the greatest control over it. One group of models assumes that solidification occurs at the inner core boundary (ICB) with essentially random crystal orientation, and that the large scale anisotropy develops later, in response to solid state convection (Jeanloz and Wenk, 1988), isostatic adjustment and compaction (Sumita et al., 1996; Yoshida et al., 1996), or Lorentz forces associated with the geomagnetic field (Karato, 1999). Another group of models assumes preferred crystal alignment develops during the solidification process itself, and is controlled by dendritic growth along the thermal gradient (Bergman, 1997) or solid-state magnetic effects (Karato, 1993). Still another group of models supposes that the inner core has solidified as a single crystal, or as a few very large crystals with a preferred alignment (Stixrude and Cohen, 1995).

The Earth's rotation is an obvious candidate to explain the axial part of inner core anisotropy. Deviations from this symmetry in the inner core are harder to account for, because departures from axial symmetry are not observed in the fluid outer core. One possible explanation for nonaxisymmetry in inner core texture is that azimuthal variations in the structure of the lower mantle have a long-term effect on inner core growth. For example, Sumita and Olson (1999) suggested that thermal coupling of the inner core to the heterogeneous mantle could provide a mechanism for producing hemispherical variations in inner core structure.

In this paper, we investigate the influence of environmental factors found in the Earth's core on compressional wave anisotropy in directionally solidified gallium. Although the properties of gallium differ from the iron-rich inner core in some important respects, several of the critical dimensionless parameters that characterize core material, including the Prandtl and the magnetic Prandtl number, are comparable to gallium (see Table 1). Gallium has a low melting point ($\simeq 29\,°C$) and low vapor pressure, and gallium crystals are strongly anisotropic, making it possible to detect subtle differences in anisotropy caused by environmental factors. In addition the low viscosity and high electrical conductivity of liquid gallium allow us to achieve high Reynolds and Hartmann numbers in our experiments (see Table 2), the dynamical regime of the fluid outer core. Two potentially important limitations of our study should be noted. One limitation is that we restrict our attention to solidification of (essentially) pure gallium liquid. We do not consider crystallization from a multicomponent liquid. This is potentially a significant limitation in the application of our results, since it is likely that the fluid outer and the solid core are not purely iron, but instead are both iron-rich compounds (Stixrude et al., 1997). The difference in texture of sea ice and lake ice (Weeks and Gow, 1978) is a well-established example of directional crystallization in single component versus multicomponent geophysical fluids. The anisotropy of directionally solidified binary alloys has been measured by Bergman (1997) and Bergman et al. (2000), who observe dendrite formation and ultrasonic anisotropy controlled by the direction of growth. Although we do not observe dendrites, our anisotropy measurement results agree with Bergman et al. (2000) in several respects. The other possibly important limitation of this study is that the anisotropy we measure is due only to the primary fabric developed during solidification. Post-solidification texture changes, which may be important in the inner core, are insignificant here.

2. Experimental methods

We use nearly pure (99.99%) gallium as our solidifying metal. The relevant physical properties of the solid and liquid phases of gallium are listed in Table 1, and some critical dimensionless experiment parameters are listed in Table 2, along with estimates of their values in the core.

Table 1
Physical properties of liquid and solid gallium

Physical property	Symbol	Units	Value
Liquid gallium			
Density	ρ	kg/m^3	6.095×10^{3}[a,b]
Dynamic viscosity	μ	kg/(m s)	1.96×10^{-3}[a], 1.8×10^{-3}[b]
Kinematic viscosity	$\nu = \mu/\rho$	m^2/s	3.22×10^{-7}[a], 2.95×10^{-7}[b]
Melting temperature	T_{f}	°C	29.771[b], 29.78[c], 29.76[d]
Boiling temperature	T_{e}	°C	2203[c], 2204[d]
Thermal expansion coefficient	α	K^{-1}	1.26×10^{-4}[e]
Thermal conductivity	k	W/(m K)	30.6[e] (at 30 °C), 28.68[b] (at 77 °C)
Specific heat	C	(J/kg K)	381.5[b], 397.6[f]
Thermal diffusivity	$\kappa = k/\rho C$	m^2/s	$1.18 \times 10^{-5} \leq \kappa \leq 1.36 \times 10^{-5}$
Prandtl number	Pr	ν/κ	$0.022 \leq Pr \leq 0.027$
Electrical conductivity	σ	(mΩ)$^{-1}$	3.87×10^{6}[b], 3.85×10^{6}[c]
Magnetic diffusivity	$\lambda = 1/\mu_0\sigma$	m^2/s	0.21
Magnetic Prandtl number	P_{m}	ν/λ	$1.4 \times 10^{-6} \leq P_{m} \leq 1.53 \times 10^{-6}$
Compressional wave velocity	V_P	m/s	2873[h] (at 30 °C), 2860[i] (at 30 °C)

	Crystal axis		
	a	b	c
Solid gallium, Ga$_\alpha$			
Length (nm)	0.45186[b]	0.45258[b]	0.76602[b]
Thermal conductivity k (W/(m K))	88.4[b]	40.8[b]	16.0[b]
Electrical conductivity σ ((mΩ)$^{-1}$)	12.3×10^{6}[b]	5.7×10^{6}[b]	1.8×10^{6}[b]
Latent heat of fusion L (kJ/kg)		79.8[b], 80.16[c]	
Compressional wave velocities V_P (m/s)	4080[f], 4151[g]	3860[f], 3948[g]	4760[f], 4823[g]

[a] Spells (1936).
[b] Sabot and Lauvray (1995).
[c] Cubbery (1979).
[d] Lide (1995).
[e] Okada and Ozoe (1992).
[f] Roughton and Nash (1962).
[g] Lyall and Cochran (1971).
[h] Beyer and Ring (1972).
[i] Brito et al. (2001).

Table 2
Dimensionless physical parameters of the various crystallization experiments of gallium[a]

Parameter	Definition	Experiments numbers	Value	Earth's core
Prandtl number	$Pr = \nu/\kappa$	1: 1–18, 31–38; 2: 6–8, 10, 14, 17	0.025	0.02
Magnetic Prandtl number	$P_{m} = \nu/\lambda$	1: 19–30; 2: 11—14, 16	1.5×10^{-6}	10^{-5}
Rayleigh number	$Ra = \alpha g \Delta T D^3/\kappa\nu$	1: 1–30; 2: 6–8, 10, 11–14, 16, 17	4–7×10^5	$\sim 10^{20}$
Reynolds number	$Re = \omega D^2/\nu$	2: 1–5, 7, 9, 15	400	10^7
Peclet number	$Pe = \omega D^2/\kappa$	2: 1–5, 7, 9, 15	10	2×10^5
Magnetic Reynolds number	$R_{m} = \omega D^2/\lambda$	1: 19–30; 2: 11–14, 16	6×10^{-4}	10^2
Hartmann number	$Ha = BD(\sigma/\rho\nu)^{1/2}$	1: 19–30; 2: 11–14, 16	2–4×10^2	10^8

[a] In column "experiments numbers" 1 and 2 stands for type-1 and type-2 experiments, respectively (see Section 2.3 and Figs. 9–13).
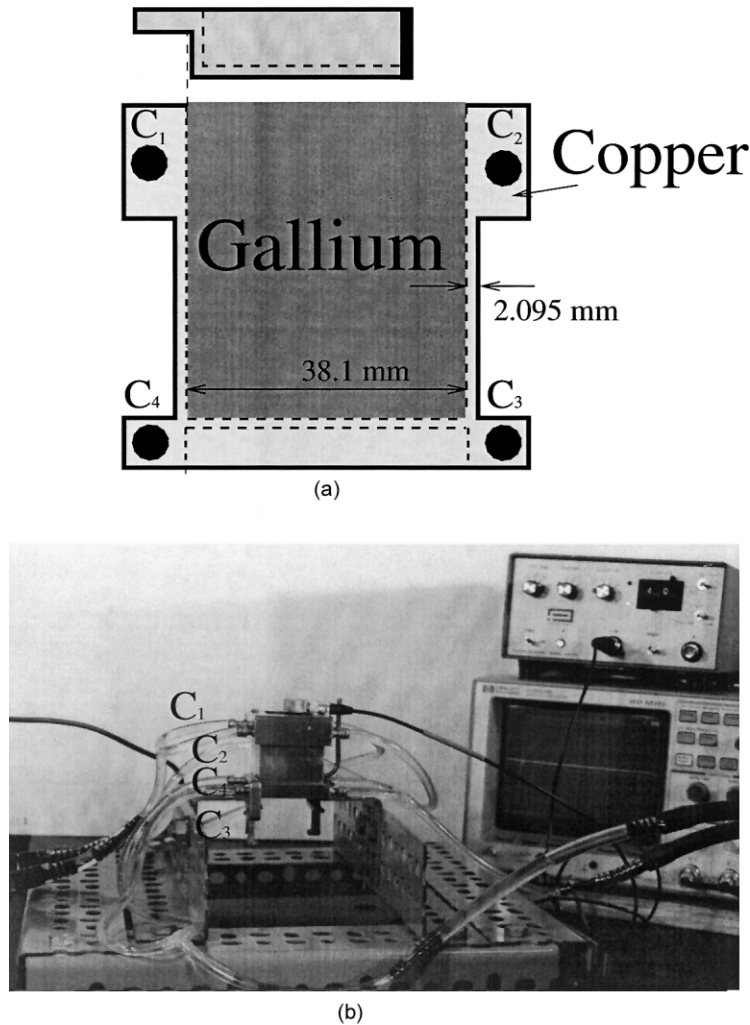
Fig. 1. Experimental apparatus (a) diagram of the copper crystallization chamber; (b) Photograph of the set-up. The ultrasonic pulse generator is connected to a transducer located at the top of the chamber. In this configuration, the transducer measures V_P in the vertical direction. Temperature boundary conditions are imposed by circulating cooling fluids through the manifolds C_1–C_4.

2.1. Apparatus

The crystallization chamber used in our experiments is shown in Fig. 1a. It consists of a copper cube with interior linear dimensions of 38.1 mm and wall thickness of 2.095 mm. The chamber lid was designed with slightly smaller dimensions than the cube and fastened with spring-loaded screws, in order to allow volume expansion of the gallium during solidification. Fluid from two thermostated baths are circulated through two of the four manifolds labeled C_1, C_2, C_3, C_4 in Fig. 1a and b. Using different combinations of the manifolds, we are able to impose either horizontal or vertical thermal gradients, and convectively stable or unstable thermal stratification in the melt.

2.2. Ultrasonic velocity measurement technique

We use ultrasound to measure in situ the compressional wave speed V_P in both the solid and liquid

phases of the gallium. Compressional wave speeds as a function of direction, position and time are used to determine the elastic anisotropy and also to track the motion of the liquid–solid interface during directional solidification.

Our two-probe technique for determining the wave speed along a given direction of the cube is illustrated in Fig. 2. A compressional ultrasonic transmitter and receiver pair (usually 5 MHz transducers, Panametrics model V126RM) are attached to opposing faces of the cube. Signals from a 35 MHz pulse generator (Panametrics model 5072PR) are recorded via a 60 MHz digital oscilloscope (HP model 54603B) and analyzed on a lab PC.

Schematic ultrasound ray paths are shown in Fig. 2b and a shows an ultrasound record from liquid gallium, including the source pulse and three receiver pulses,

corresponding to the arrivals labeled $t_1 - t_3$ in Fig. 2b. The reverberations in the individual arrivals correspond to internal reflections in the copper chamber walls, as illustrated in the sketch. Fig. 2c shows superposition of the t_1 arrival with a 0.88 μs time shift, and Fig. 2d and e show the record near the first and second arrivals with a 26.6 μs time shift superimposed. The reverberation time in the copper walls is 0.88 μs and the propagation time through the gallium is 26.6 μs. From these we obtain V_P(Cu) = 4723 ± 64 m/s and V_P (Ga liquid) = 2865 ± 12 m/s. The first value is within experimental uncertainty for the type of copper used (4660 m/s; Nondestructive Testing Handbook, 1991) and the second value is in full agreement with other determinations of V_P in liquid gallium (see Table 1).

The pulse-echo technique illustrated in Fig. 3 was used to measure the variation in wave speed with
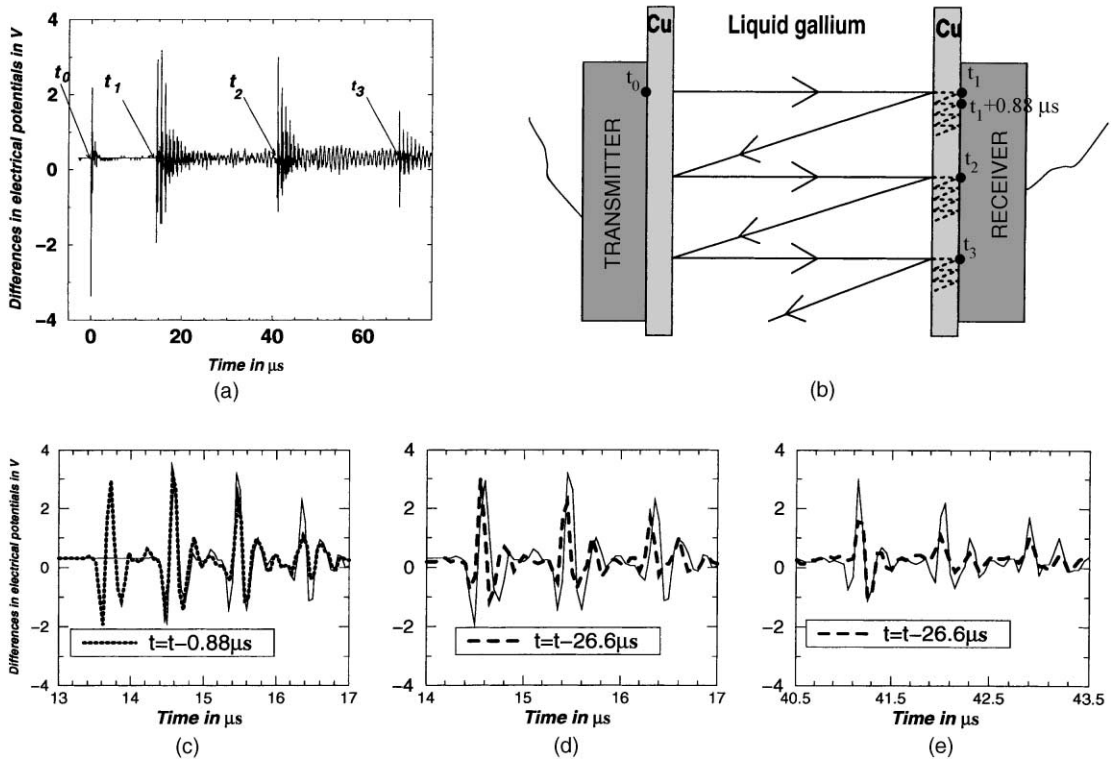

Fig. 2. Two-probe pulse-echo technique for ultrasound velocity measurements in liquid gallium. (a) Trasmitter pulse emited at time $t = t_0$ and received at time $t = t_1$; (b) Raypaths for ultrasonic wave through liquid gallium and copper chamber walls; (c), (d), (e) Tim shift of the signal autocorrelation gives reverberation time in the copper walls (0.88 μs) and propagation time through liquid gallium (26.6 μs); the original signal is the solid line and the shifted signals are the dotted and dashed lines.
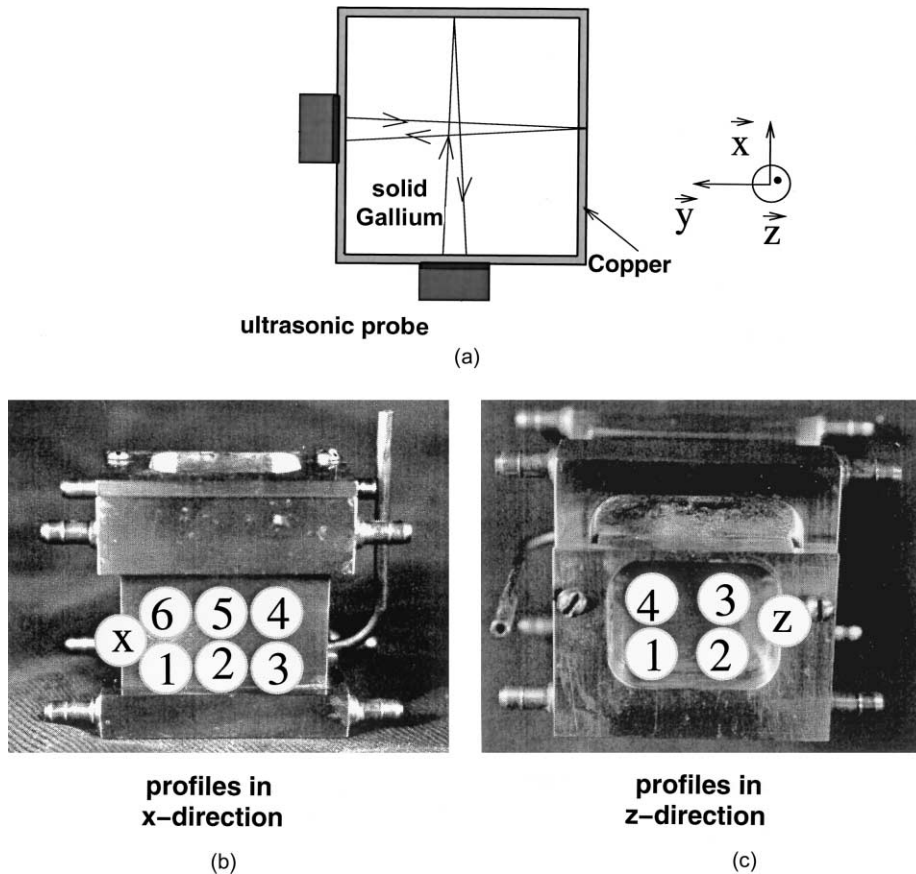
Fig. 3. Measurement of V_P in gallium solidified in the copper chamber. (a) Single probe technique, with the travel time of the direct and reflected waves giving the compressional velocity; (b) V_P measured along six different paths in both x- and y-directions to determine heterogeneity in anisotropy; (c) Four paths are measured in the z-direction.

position and with direction after solidification. Two-way travel times were measured at six positions on the x- and y-faces and four positions on the z-face of the cube. By varying the direction of source and receiver transducer pairs, we obtain information on directional variations in wave speed; by varying their location along a given direction, we obtain information on heterogeneity in wave speed along that direction.

Several different average velocities are calculated. First, we compute the face–average velocity, by averaging the velocities measured along the parallel ray paths of a single sample. This gives the average anisotropy of each sample. However, this may not give a good estimate of the true anisotropy.

Given the size of our crystallization chamber and the characteristic grain size of the solid, each individual ray path samples only a relatively small number of grains of the solid (we estimate 3–6 grains along a typical path). Averages over six parallel paths taken at different locations on a given face then gives us an effective sample average over roughly 18–36 grains. However, previous texture studies (Nicolas and Poirier, 1976) have concluded a larger number of grains, of the order 100, must be sampled on a ray path to reliably estimate the anisotropy. The individual grains in our samples were too large (compared to the sample size) for this minimum sampling criterion to be met for any single sample. In order to overcome this limitation, we also calculate face–average velocities
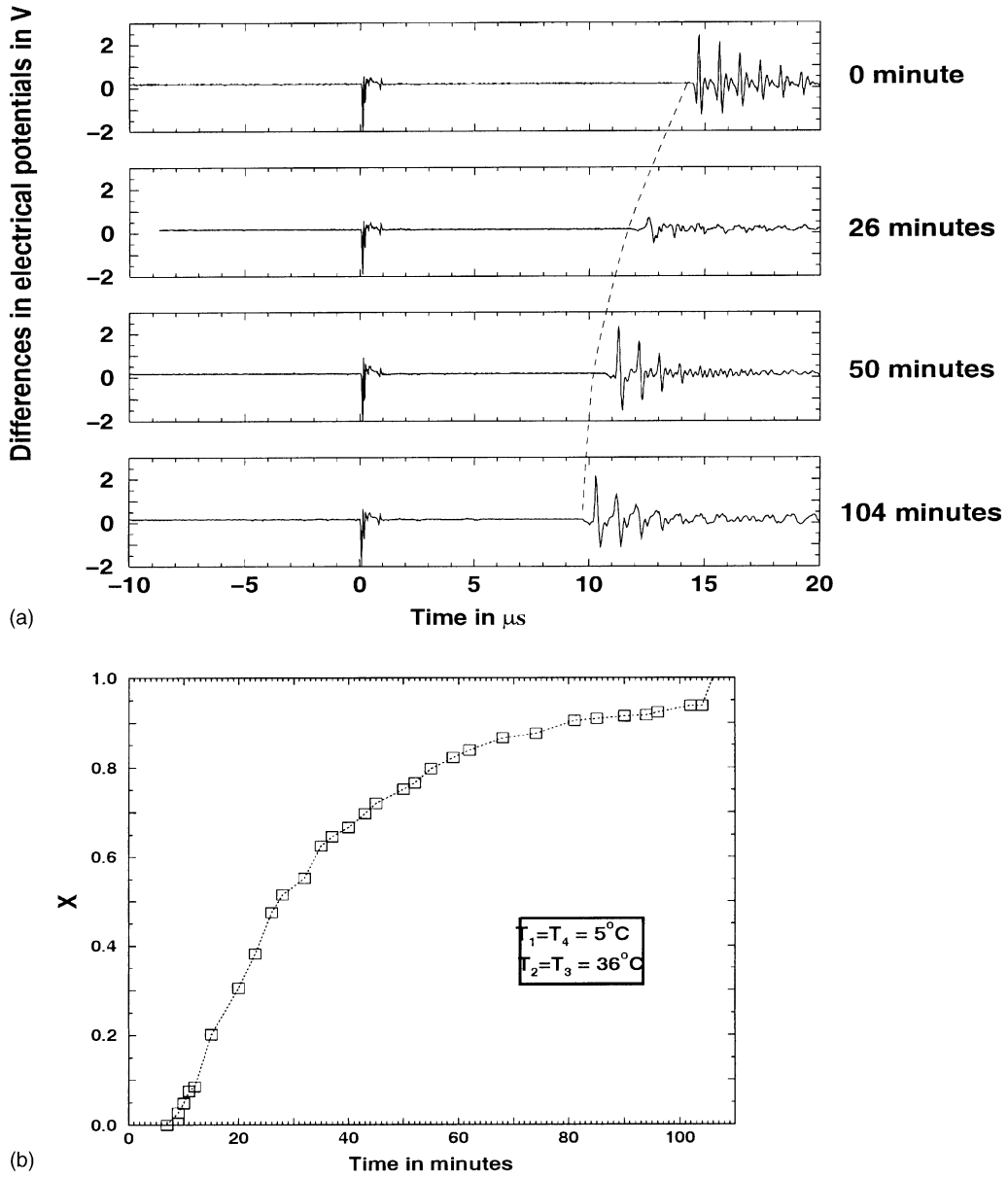
Fig. 4. Ultrasonic measurement using the two-probe technique, in an experiment with horizontal directional solidification. $T_1 = T_4 = 5\,^{\circ}$C and $T_2 = T_3 = 36\,^{\circ}$C: T_1, T_2, T_3 and T_4 are the temperature of the water circulating through the manifolds C_1, C_2, C_3 and C_4 (see Fig. 1), respectively. (a) Ultrasonic signal after 0, 26, 50 and 104 min. The dotted line indicates the first arrivals; (b) $X = (D_{\mathrm{solid\,gallium}}/D_{\mathrm{box}})$ ratio during the experiment, $D_{\mathrm{solid\,gallium}}$ being the position of the liquid–solid interface and D_{box} the total length of the copper box.

over multiple solid run products, obtained by repeating the experiment with the same external and initial conditions. By repeating the same experiment five times or more, with six ray paths measured on each set of faces, the directional velocities are effective determined as averages over about 100 different grains.

For most of the velocity determinations, we used the autocorrelation method over the whole record to determine the travel times, instead of the arrival times of individual phases. Arrival times picks of individual phases can be biased by internal reflections and scattering effects. Grain boundary scattering is potentially an important source of bias in our experiments, since the grain size is comparable to the ultrasound wavelength. In order to minimize its influence, we report travel times and velocities derived from autocorrelation maxima, which is rather insensitive to scattered energy.

In addition to velocity determinations, we were able to follow the propagation of the liquid–solid interface, using the ultrasonic technique illustrated in Fig. 2. Fig. 4 shows records from an horizontal solidification experiment at four separate times, including both the transmitter and receiver pulses. The transmitter and receiver were in the positions shown in Fig. 2, and a horizontal thermal gradient was imposed so the solidification progressed from left to right across the chamber. Fig. 4a shows the moveout in the arrival time of the direct wave across the sample as the amount of higher velocity, solid material increases. Using the travel times and velocities for solid and liquid gallium phases listed in Table 1, we calculate the position of the liquid–solid interface versus time. The results for this particular experiment are shown in Fig. 4b. Following an initial delay time of about 10 min for nucleation, the displacement of the solidification interface increases as the square root of time, in accord with theoretical predictions from the Stefan model for solidification front propagation through an infinite fluid half pace (Turcotte and Schubert, 1982).
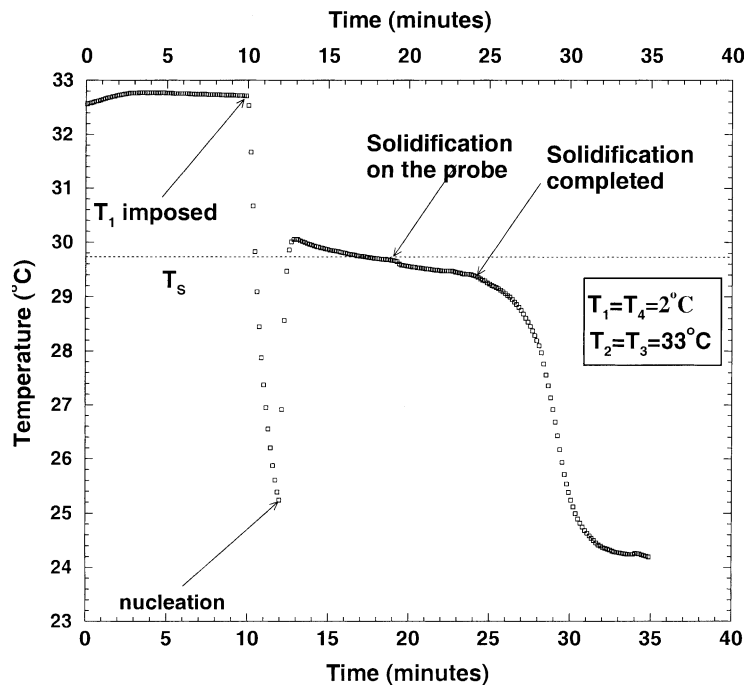

Fig. 5. Temperature measurements during horizontal solidification. Boundary temperatures are $T_1 = T_4 = 2\,°C$ and $T_2 = T_3 = 33\,°C$. Solidification temperature of gallium T_s is indicated by a dotted line. The time at which T_1 was imposed, the initiation of nucleation, the time at which the solidification reached the temperature probe, and the end of solidification are all indicated.

2.3. Initial conditions

We experimented with two different initial conditions. In type-1 experiments, the liquid gallium was removed and the chamber cleaned after each run. Each experiment of this type began by pouring entirely liquid gallium into a chamber free of solid nucleation grains and then applying the temperature boundary conditions to initiate directional solidification, along with the other external controls. Experiments of this type generally required about 1 h to complete. In type-2 experiments, the gallium was not removed from the chamber between runs. Instead, the solid product was simply re-melted in situ using the thermostatic temperature control system, and new external conditions were applied to begin the next run. These experiments took less time to prepare and less time to complete than the type-1 experiments, because a few small solid grains of gallium and gallium oxides remained in the chamber and provided sites to initiate crystal nucleation. We emphasize this difference in initial conditions because we find it is the single most important factor in controlling the onset of solidification and the resulting elastic anisotropy of the solid.

To illustrate this point, Fig. 5 shows liquid temperature versus time measured in the gallium along the line of horizontal solidification from a type-2 experiment, without cleaning the chamber. The times when the thermal gradient was imposed, nucleation initiated, solidification front reached the probe, and solidification was completed are all indicated on the figure. The rates of solidification in Fig. 5 differ substantially from the rates shown in Fig. 4, a type-1 experiment with an initially cleaned chamber. In the type-2 experiments (Fig. 5) the interface propagates nearly linearly with time, in contrast to the square root of time propagation seen in type-1 (Fig. 4). In addition, the onset time for nucleation and the time required to complete solidification are much shorter for type-2 (Fig. 5) than for type-1 (Fig. 4). Evidently the initial presence of nucleation grains affects every stage of the solidification.

3. Experimental results

3.1. Crystal growth characteristics

Solid gallium run-products were investigated for each type of crystallization experiment. Character-

ization included identification of gallium polymorphy, grain structure, preferred orientation, and contamination using X-ray diffraction, backscattered-electron imaging and reflected-light microscopy.

Gallium crystallization is characterized by sluggish nucleation and usually requires extensive supercooling. Because a metastable polymorph of gallium (space group Cmcm) has been reported in supercooled experiments (Curien et al., 1961), we limited our supercooling to about 10 °C and verified the presence of the stable, alpha-gallium phase (orthorhombic; space group Cmca) by X-ray diffraction. Fig. 6 shows run products from two typical experiments. The samples have been partially re-melted along their faces to facilitate removal from the chamber.

Fig. 6a and b are side- and top-views, respectively, of a gallium block crystallized in a vertical temperature gradient. In Fig. 6a, the boundary between two grains has been highlighted by oblique lighting. This boundary is seen to extend the entire length of the block and is fairly straight. The vector $\vec{q}$ drawn on the sample indicates the direction of conductive heat flow and the solidification direction. As expected, the grains are elongated parallel to the heat flow vector.

Fig. 6b shows that the grain structure transverse to the heat flow is more complex. To reveal this structure, the top of the sample was hand polished with wenol compound and then lightly etched with an HCl–alcohol mixture. Note that the block comprises only a few grains (five) and that grain boundaries across the heat-flow direction are serrate and complex.

Fig. 6c is a side-view of a gallium block crystallized in a horizontal temperature gradient. This block again shows that crystallization resulted in five grains elongated parallel to the cooling direction. Apart from heat flow, we did not detect any control on grain elongation from other externally imposed factors. In particular, the direction of gravity, externally imposed magnetic fields and forced convection in the liquid all had no measurable effect on grain shape.

We have also determined the relationship between grain shape and the crystallographic orientation. Oriented slivers of samples were investigated by X-ray precession to identify crystallographic axis directions. The slivers were approximately 1 mm long and extracted with a scalpel. Samples were refrigerated to $\simeq 3$ °C prior to scalpel extraction. Results of
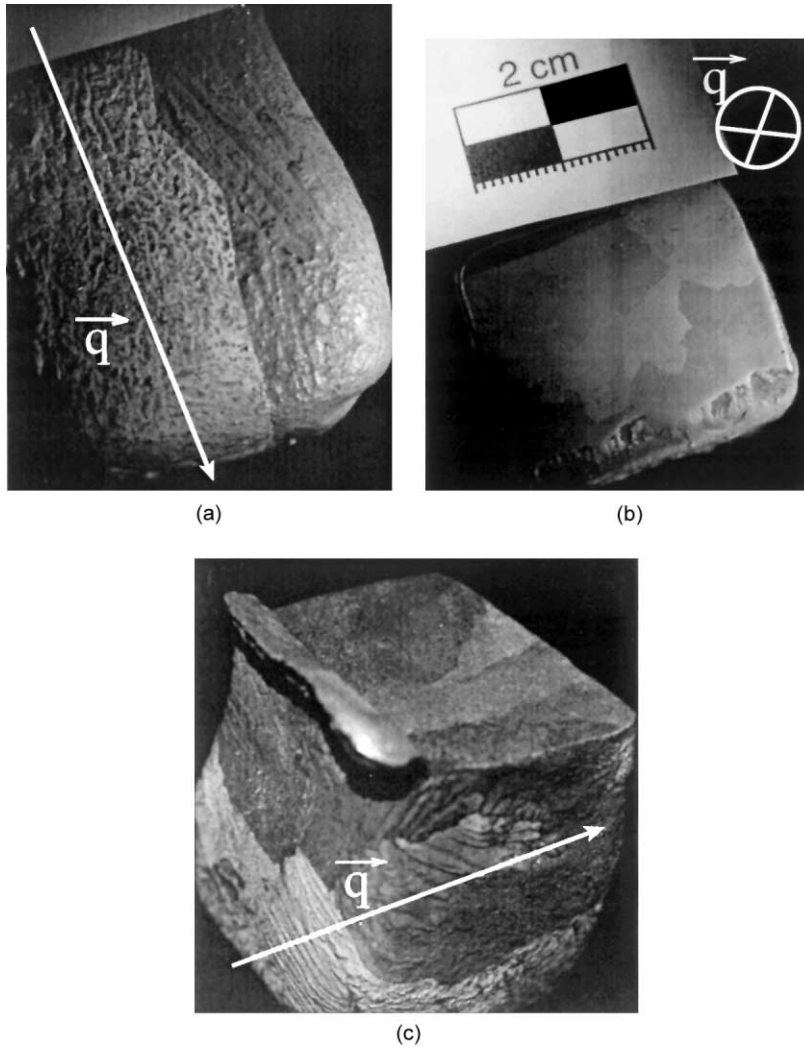
Fig. 6. Photographs showing texture development in directionally solidified gallium from two samples extracted at the end of solidification. (a), (c) Grains are elongated sub-parallel to the heat flow direction (labeled $\vec{q}$); (b) Same sample as (a) with a section taken perpendicular to the heat flux vector.

orientation analysis reveal that grain elongation and, therefore, growth direction do not coincide with particular symmetry directions of the gallium. This possibly surprising result is, in fact, fundamental to understanding the anisotropy results in the next section.

Variable crystallographic orientation accounts for the substantial spread in acoustic anisotropy in Figs. 9–13. Only a few individual experiments show acoustic anisotropy close to that of single crystals.

These few experiments are the only ones with principal axes parallel to growth. It appears that, in general, nucleation in gallium is difficult enough that the crystallographic orientation is controlled mostly by the initial nuclei rather than intensive thermodynamic parameters. This behavior is consistent with the large supercooling in pure gallium. It is not certain whether a multicomponent alloy such as the Earth's core will solidify with the same supercooling, and would be similarly sensitive to initial nuclei.
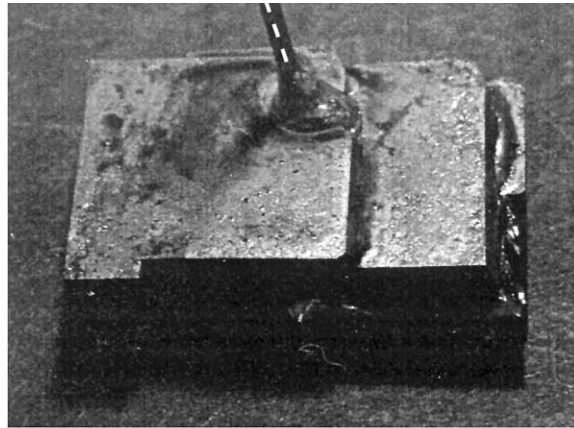
(a)
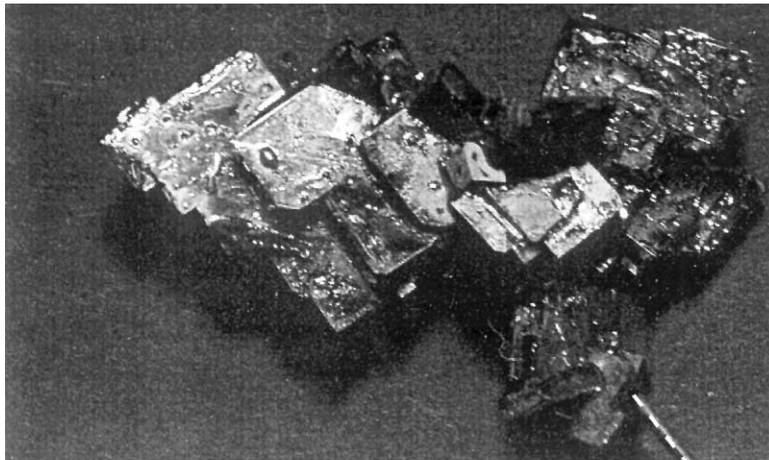
(b)

Fig. 7. Photographs of gallium polycrystals formed by plunging a rotating, seeded needle (direction indicated by a white dotted line) in supercooled gallium. A preferred orientation of the crystals is seen in both photographs, either perpendicular to the needle (a) or aligned with the needle (b). These demonstrate that the initial nucleation controls the lattice preferred orientation.

The importance of initial nuclei orientation was further investigated by crystallization using introduced seed grains. Seed crystals were created by freezing tiny droplets of gallium on the end of a needle. The seeds were then introduced into supercooled gallium while spinning at speeds ranging from 0 to 45 rev/min. In all cases, the final crystallites showed preferred orientations controlled by the seed crystal. Fig. 7 shows the result of two such experiments and highlights the strong crystallographic control.

Finally, minor copper contamination of the gallium was noted in runs involving cycled crystallization without replacement with fresh gallium. We were aware that copper has extensive solution in gallium (Subramanian and Laughlin, 1990) and the use of a copper apparatus might be problematic. Despite this concern, our experiments never had more than a trace of copper–gallium contamination. Contaminants were small ($<100\,\mathrm{m}$), euhedral to subhedral crystals of $CuGa_2$ and were always found encased in large, single crystals of pure gallium with no spatial association to nucleation sites or grain boundaries.

One might expect that solidification in the binary system Ga–Cu could be complicated by constitutional
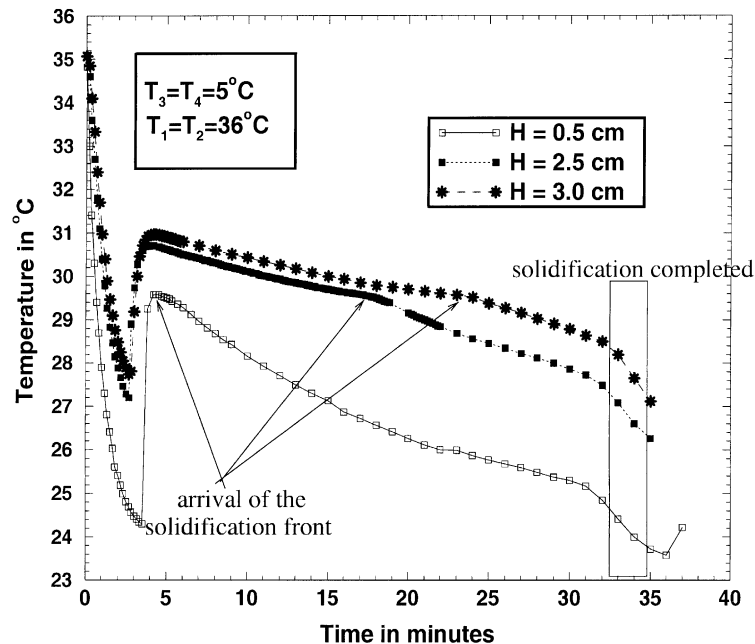
Fig. 8. Temperatures measured in situ at different heights in the chamber during three experiments with vertical solidification. $T_1 = T_2 = 36\,°C$ and $T_3 = T_4 = 5\,°C$. H is measured with respect to the bottom of the box.

supercooling and associated formation of a dendritic microstructure at the solid–liquid interface. However, the extremely small degree of copper contamination and the low temperatures of investigation prevented this complication in our experiments. In accordance with published phase relations (Subramanian and Laughlin, 1990), the gallium metal in our run products was essentially pure and there is no meaningful fractionation between the binary liquid and the solidification products. More directly, we never observed acoustic scattering attributable to a mushy zone during solidification, nor any relict microstructure in the solidified blocks. In short, we found no evidence that copper contamination played a role in the final acoustic anisotropy of the experiments.

3.2. Temperature measurements

Fig. 8 shows the temperature measured at different heights during a vertical cooling experiments. The temperature curves indicate that the gallium liquid undergoes a supercooling phase prior to initial nucleation, a characteristic of pure metallic fluids, espe-

cially ones with low melting points (Reed-Hill, 1973). Once nucleation begins, latent heat of solidification is released and the temperature of fluid increases above the melting point, as shown in Fig. 8. We observe the same behavior in the temperature curves at all heights. After the initial nucleation, temperature is barely above the solidification temperature, indicating the probe is surrounded by melt. Later there is a break in slope in the temperature curve, indicating the arrival of the propagating solidification front. In the final phase, the solidification is complete, the latent heat contribution vanishes, (after about 32 min in Fig. 8) and the rate of cooling increases.

4. Anisotropy measurements

In order to determine how some of the environmental factors proposed to explain the inner core anisotropy may affect the initial texture in metals undergoing directional solidification, we have measured the compressional wave speed V_P versus direction and position in directionally solidifying gallium

Table 3
Ultrasonic measurements of V_P shown in Figs. 9–12[a]

Ultrasonic measurements in solid gallium after crystallization

#	V_x			V_y			V_z			Experimental conditions
1	4239.94	7.55	11.3	4265.75	17.55	18.26	4432.18	8.38	7.09	V, $T_3 = T_4 = 5\,°C$, $T_1 = T_2 = 40\,°C$
2	4196.04	6.93	9.23	3949.76	50.24	44.07	4571.29	41.3	32.88	V, $T_3 = T_4 = 5\,°C$, $T_1 = T_2 = 40\,°C$
3	4636.48	15.53	15.5	4222.21	11.13	7.6	4277.31	10.81	13.18	V, $T_3 = T_4 = 5\,°C$, $T_1 = T_2 = 40\,°C$
4	3918.19	44.37	22.48	4517.08	92.72	63.55	4236.95	20.04	20.01	V, $T_3 = T_4 = 3\,°C$, $T_1 = T_2 = 36\,°C$
5	4383.53	10.94	14.26	4191.17	28.1	34.05	4244.64	19.48	34.7	V, $T_3 = T_4 = 5\,°C$, $T_1 = T_2 = 36\,°C$
6	4263.03	27.51	27.34	4203.01	16.26	9.28	4558.28	93.73	83.83	V, $T_3 = T_4 = 5\,°C$, $T_1 = T_2 = 36\,°C$
7	4227.23	29.75	33.5	4654.9	14.22	14.22	4189.92	17.69	14.58	V, $T_3 = T_4 = 5\,°C$, $T_1 = T_2 = 36\,°C$
8	4296	38.47	39.02	4119.83	8.02	14.22	4419.1	76.48	128.56	V, $T_3 = T_4 = 5\,°C$, $T_1 = T_2 = 36\,°C$
9	4132.71	77.23	172.21	4363.11	113.98	62.88	4353.24	28.59	48.16	H, $T_1 = T_4 = 5\,°C$. $T_2 = T_3 = 36\,°C$
10	4261.9	28.64	30.91	4413.42	29.73	39.14	4309.31	30.09	35.62	H, $T_1 = T_4 = 5\,°C$, $T_2 = T_3 = 36\,°C$
11	4320.99	129.94	179.69	4458	171.41	174.69	4158.51	46.79	37.36	H, $T_1 = T_4 = 5\,°C$, $T_2 = T_3 = 36\,°C$
12	4221.03	31.2	38.81	4424.69	26.24	55.43	4150.39	15.82	15.82	H, $T_1 = T_4 = 5\,°C$, $T_2 = T_3 = 36\,°C$
13	4362.98	194.43	180.77	4177.12	84.62	71.52	4341.29	10.51	16.65	H, $T_1 = T_4 = 5\,°C$, $T_2 = T_3 = 36\,°C$
14	4269.13	31.09	31	4359.57	93.96	76.27	4437	37.46	37.46	H, $T_1 = T_4 = 5\,°C$, $T_2 = T_3 = 36\,°C$
15	4052.56	46.41	42.04	4458.16	137.73	259.82	4197.2	8.1	8.08	H, $T_1 = T_4 = 15\,°C$, $T_2 = T_3 = 35\,°C$
16	4074.54	39.93	19.19	4560.82	46.19	43.92	4204.74	9.87	11.01	H, $T_1 = T_4 = 15\,°C$, $T_2 = T_3 = 35\,°C$
17	4401.38	44.36	37.12	4120.43	45.78	36.83	4398.28	11.44	8.88	H, $T_1 = T_4 = 15\,°C$, $T_2 = T_3 = 35\,°C$
18	4497.02	60.39	61.63	3894.1	31.71	12.29	4242.85	21.28	18.9	H, $T_1 = T_4 = 15\,°C$, $T_2 = T_3 = 35\,°C$
19	4261.95	38.28	33.31	4182.22	4.59	2.3	4471.99	36.88	26.25	V, $T_3 = T_4 = 5\,°C$, $T_1 = T_2 = 36\,°C$, $B_z = 600\,G$
20	4045.31	10.03	7.16	4185.19	22.43	32.6	4714.45	24.35	22.33	V, $T_3 = T_4 = 5\,°C$, $T_1 = T_2 = 36\,°C$, $B_z = 600\,G$
21	4026.93	105.39	117.24	4259.02	65.61	60.67	4542.81	97.87	102.25	V, $T_3 = T_4 = 5\,°C$, $T_1 = T_2 = 36\,°C$, $B_z = 600\,G$
22	4375.88	127.66	75.66	4008.17	36.42	53.83	4343.22	110.31	172.45	V, $T_3 = T_4 = 5\,°C$, $T_1 = T_2 = 36\,°C$, $B_z = 600\,G$
23	4160.66	65.63	35.05	4057.79	38.99	43.03	4581.45	81.95	83.22	V, $T_3 = T_4 = 5\,°C$, $T_1 = T_2 = 36\,°C$, $B_z = 600\,G$
24	4315.15	94.57	72.39	4118.93	6.68	6.68	4185.77	56.99	53.45	V, $T_3 = T_4 = 5\,°C$, $T_1 = T_2 = 36\,°C$, $B_z = 1200\,G$
25	4586.7	85.28	176.98	4002.64	35.51	29.75	4213.73	52.78	42.96	V, $T_3 = T_4 = 5\,°C$, $T_1 = T_2 = 36\,°C$, $B_z = 1200\,G$
26	4109.62	123.71	90.64	4536.96	78.42	49.33	4294.78	7.88	6.65	V, $T_3 = T_4 = 5\,°C$, $T_1 = T_2 = 36\,°C$, $B_z = 1200\,G$
27	4206.18	27.15	26.26	4183.99	39.96	38.18	4245.13	2.37	2.36	V, $T_3 = T_4 = 5\,°C$, $T_1 = T_2 = 36\,°C$, $B_x = 600\,G$
28	4262.14	102.12	109.55	4380.88	88.33	128.65	4168.4	141.55	71.63	V, $T_3 = T_4 = 5\,°C$, $T_1 = T_2 = 36\,°C$, $B_x = 600\,G$
29	4218.95	180.59	124.38	4357.56	153.99	154.58	4106.28	21.56	33.59	V, $T_3 = T_4 = 5\,°C$, $T_1 = T_2 = 36\,°C$, $B_x = 600\,G$
30	4139.07	59.28	57.6	4453.06	74.57	61.13	4147.94	45.79	68.71	V, $T_3 = T_4 = 5\,°C$, $T_1 = T_2 = 36\,°C$, $B_x = 600\,G$
31	4234.09	90.54	132.9	4372.56	39.72	60.16				U at $T = 20\,°C$
32	4271.07	229.82	154.38	4103.73	71.61	99.52				U at $T = 20\,°C$
33	4199.31	45.82	30.82	4481.84	75.57	157.21				U at $T = 20\,°C$
34	4392.4	186.93	226.19	4169.91	49.36	121.03				U at $T = 25\,°C$
35	4231.29	110.59	165.13	4382.35	58.21	125.36				U at $T = 25\,°C$
36	4249.14	135.21	278.33	4370.21	39.51	23.38				U at $T = 25\,°C$
37	4303.95	272.63	140.02	4238.38	47.34	63.04				U at $T = 25\,°C$
38	4276.28	153.95	207.92	4142.14	58.52	84.63				U at $T = 25\,°C$

[a] For each direction x, y and z, respectively, the first column is the average value of V_P, the second column is the difference between the averaged value and the minimum measured value, and the third column is the difference between the averaged value and the maximum value. The last column of the table lists the experimental conditions: V denotes experiments with vertical gradient of temperature, H denotes experiments with horizontal gradient of temperature and U denotes experiments with uniform gradient of temperature. T_1, T_2, T_3, and T_4 are the temperature of the water circulating through the manifolds C_1, C_2, C_3 and C_4, respectively (see Fig. 1). B_x denotes a horizontal imposed magnetic field (along the x-direction in Fig. 3) and B_z denotes a vertical imposed magnetic field.

Table 4
Ultrasonic measurements of V_P shown in Fig. 13[a]

Ultrasonic measurements in solid gallium after crystallization

#	V_x			V_y			V_z			Experimental conditions
1	4045.06	42.92	28.2	4136.81	2.25	2.25	4504.9	14.67	11.98	H, $T_1 = T_4 = 5\,^\circ$C, $T_2 = T_3 = 36\,^\circ$C, $\omega = 500$ rev/min
2	4275.8	24.43	23.56	4349.36	17.41	14.89	4584.92	36.06	102.57	H, $T_1 = T_4 = 5\,^\circ$C, $T_2 = T_3 = 36\,^\circ$C, $\omega = 500$ rev/min
3	4246.9	43.64	92.05	4352.31	27	32.58	4466.84	28.74	46.89	H, $T_1 = T_4 = 5\,^\circ$C, $T_2 = T_3 = 36\,^\circ$C, $\omega = 500$ rev/min
4	4572.55	23.35	28.72	4127.32	38.9	32.74	4164.02	22.79	29.46	H, $T_1 = T_4 = 5\,^\circ$C, $T_2 = T_3 = 36\,^\circ$C, $\omega = 500$ rev/min
5	4535.46	54.9	47.83	4305.66	36.22	29.57	4293.11	36.44	33.75	H, $T_1 = T_4 = 5\,^\circ$C, $T_2 = T_3 = 36\,^\circ$C, $\omega = 500$ rev/min
6	4204.86	149.42	79.26	4208.67	50.69	51.55	4421.53	24.21	62.26	H, $T_1 = T_4 = 5\,^\circ$C, $T_2 = T_3 = 36\,^\circ$C, $\omega = 0$
7	4415.76	128.07	103.37	4378.91	15.55	9.65	4094.57	42.24	77.7	H, $T_1 = T_4 = 5\,^\circ$C, $T_2 = T_3 = 36\,^\circ$C, $\omega = 500$ rev/min
8	4651.61	31.86	33.42	4157.61	45.37	16.31	4562.97	32.93	24.55	H, $T_1 = T_4 = 5\,^\circ$C, $T_2 = T_3 = 36\,^\circ$C, $\omega = 0$
9	4197.2	8.09	10.39	4265.73	10.37	6.37	4543.84	13.57	5.43	H, $T_1 = T_4 = 5\,^\circ$C, $T_2 = T_3 = 36\,^\circ$C, $\omega = 500$ rev/min
10	4230.37	38.54	27.39	4286.58	23.37	22.45	4563.93	57.05	55.06	H, $T_1 = T_4 = 5\,^\circ$C, $T_2 = T_3 = 36\,^\circ$C, $\omega = 0$
11	4130.27	117.22	102.78	4239.95	9.91	16	4649.19	14.21	11.34	H, $T_1 = T_4 = 5\,^\circ$C, $T_2 = T_3 = 36\,^\circ$C, $B_z = 600$ G
12	4162.73	70.61	193.98	4252.94	40.02	47.64	4667.71	12.88	12.85	H, $T_1 = T_4 = 5\,^\circ$C, $T_2 = T_3 = 36\,^\circ$C, $B_z = 600$ G
13	4167.77	89.22	77.59	4195.97	44.43	65.89	4487.17	48.54	33.64	H, $T_1 = T_4 = 5\,^\circ$C, $T_2 = T_3 = 36\,^\circ$C, $B_z = 600$ G
14	4006.34	143.99	54.06	4201.9	26.74	24.27	4566.33	15.75	19.79	H, $T_1 = T_4 = 5\,^\circ$C, $T_2 = T_3 = 36\,^\circ$C, $B_z = 0$, $\omega = 0$
15	4151.11	21.95	14.3	4282.35	5.77	11.05	4628	7.03	4.22	H, $T_1 = T_4 = 5\,^\circ$C, $T_2 = T_3 = 36\,^\circ$C, $\omega = 500$ rev/min
16	4208.84	15.11	24.33	4270.35	5.74	10.99	4542.03	53.87	25.13	H, $T_1 = T_4 = 5\,^\circ$C, $T_2 = T_3 = 36\,^\circ$C, $B_z = 600$ G
17	4127.89	24.7	11.19	4253.32	63.96	93.94	4623.79	5.61	8.41	V, $T_3 = T_4 = 3\,^\circ$C, $T_1 = T_2 = 36\,^\circ$C

[a] For each direction x, y and z, respectively, the first column is the average value of V_P, the second column is the difference between the averaged value and the minimum measured value, and the third column is the difference between the averaged value and the maximum value. The last column of the table lists the experimental conditions: V denotes experiments with vertical gradient of temperature, H denotes experiments with horizontal gradient of temperature and U denotes experiments with uniform gradient of temperature. T_1, T_2, T_3, and T_4 are the temperature of the water circulating through the manifolds C_1, C_2, C_3, and C_4, respectively (see Fig. 1). B_z denotes a vertical imposed magnetic field (along the z-direction in Fig. 3). Symbol ω denotes turbulent mixing generated by a small propeller rotating at 500 rev/min in the liquid.

subject to a variety of external controls. Fig. 3 shows the six probe locations used to measure the compressional wave speed along the x- and y-directions. Wave speeds were measured at four locations along the z-direction. For the most part, the measurements in this section were taken in situ, after solidification was complete. Tables 3 and 4 list the experimental conditions and the results.

4.1. Ultrasonic determination of lattice preferred orientation from solidification experiments

Figs. 9–13 summarize the results of the anisotropy measurements from solidification experiments using various external controls. The scatter in V_P parallel ray path measurements along a given direction (see Fig. 3), is represented with errors bars in these figures.

Fig. 9 shows the anisotropy resulting from directional solidification in the presence of a stabilizing vertical temperature gradient. In Fig. 9, T_3 and T_4 refer to the temperature at the bottom of the box (temperature of manifolds C_3 and C_4, see Fig. 1), T_1 and T_2 the temperature at the top (manifolds C_1 and C_2). All of these experiments produced a spatially coherent anisotropy, ranging from 20 (experiments 1 and 5) to 80% (experiments 2 and 4) of the single crystal values (see Table 1). Although we always observe large and systematic anisotropy, that is, different mean values of V_P measured along the x-, y-, and z-axes, we find that the fastest P wave axis does not always coincide with a symmetry axis of the solidification chamber, or with the direction of the imposed thermal gradient. For example, experiments 2, 3, and 4 show fastest propagation in the z-, x-, and y-direction, respectively. Some
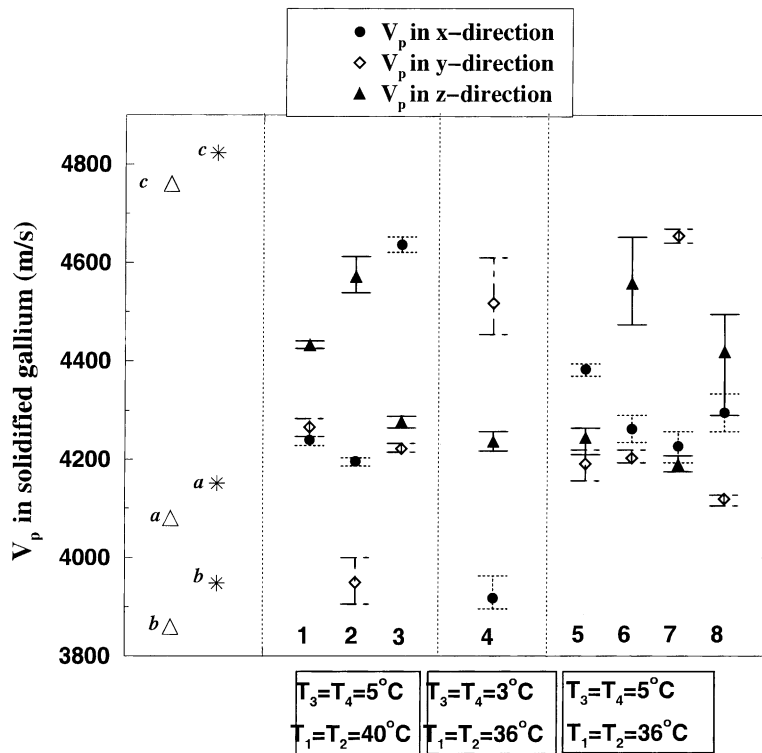

Fig. 9. Ultrasonic measurements of V_P in gallium solidified in a vertical temperature gradient, from experiments 1–8 (see Table 3). V_P is measured at six locations along the x- and y-directions and at four locations along the z-direction. Data points are the average of the locations and error bars represent the deviation around the average between the minimum and the maximum measured values. The values of V_P along the three symmetry axes of single crystal Ga$_\alpha$ are plotted for reference (see Table 1). Measurement errors are typically 50 m/s.
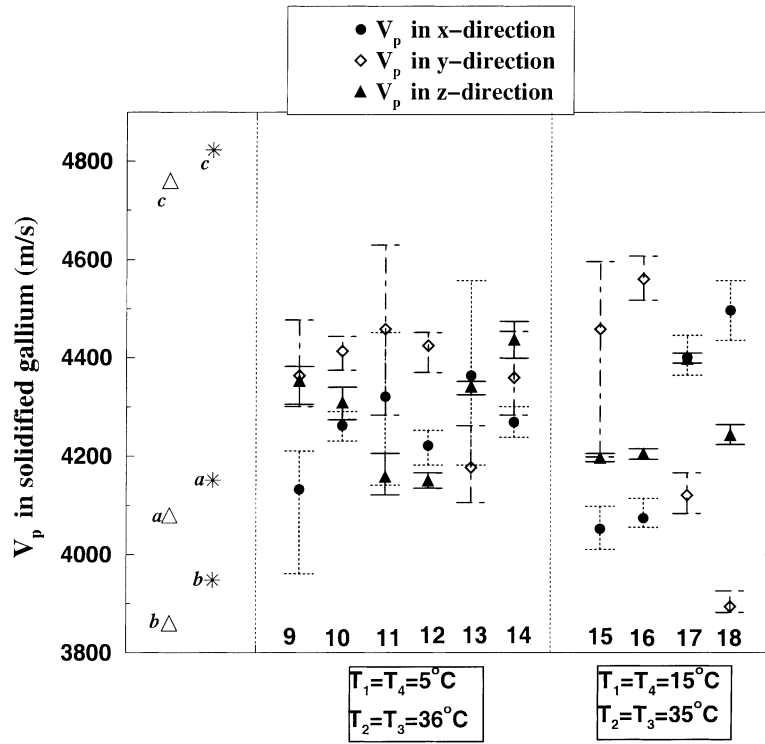
Fig. 10. Ultrasonic measurements of V_P in gallium solidified in a horizontal temperature gradient, from experiments 9–18 (see Table 3). V_P is measured at six locations along the x- and y-directions and at four locations along the z-direction. Data points are the average of the locations and error bars represent the deviation around the average between the minimum and the maximum measured values. The values of V_P along the three symmetry axes of single crystal Ga$_\alpha$ are plotted for reference (see Table 1). Measurement errors are typically 50 m/s.

experiments in Fig. 9 show very uniform anisotropy (experiment 5, for example), indicating strongly coherent crystal orientation and nearly uniform alignment of all three symmetry axes. In some cases, we obtain a transverse anisotropy, that is, isotropy in planes perpendicular to a given axis. In experiment 6 for example, V_P is isotropic and homogeneous in the x–y-plane, but the magnitude of V_P the wave speed in that plane, differs from the wave speed along the z-direction. However, these cases are somewhat the exceptions. More frequently we find anisotropy with respect to all three directions, with minor variations in anisotropy over the sample faces. Indeed, the most systematic general result from the experiments shown in Fig. 9 is that, in the presence of a stable, vertical thermal gradient, the directionally solidified gallium polycrystals have a spatially uniform anisotropy.

Fig. 10 shows the results from experiments with directional solidification driven by a horizontal temperature gradient. In these cases, crystallization occurs in an environment with free convection in the melt. Here again we measure a strong anisotropy in most of the experiments. Despite the presence of free convection in the liquid, the anisotropy of the solid does not seem to differ much from the cases with vertical cooling shown in Fig. 9. The only systematic difference we detect between these two cases is the variation in wave speed over a given face. The heterogeneity in wave speed is generally greater in Fig. 10 than in Fig. 9. This. suggests that motion in the fluid during solidification produces a more heterogeneous texture, compared to the same case with no convective motion. But this generalization does not apply to every experiment. For example, experiments 16 and 18 in Fig. 10 produced basically the same type
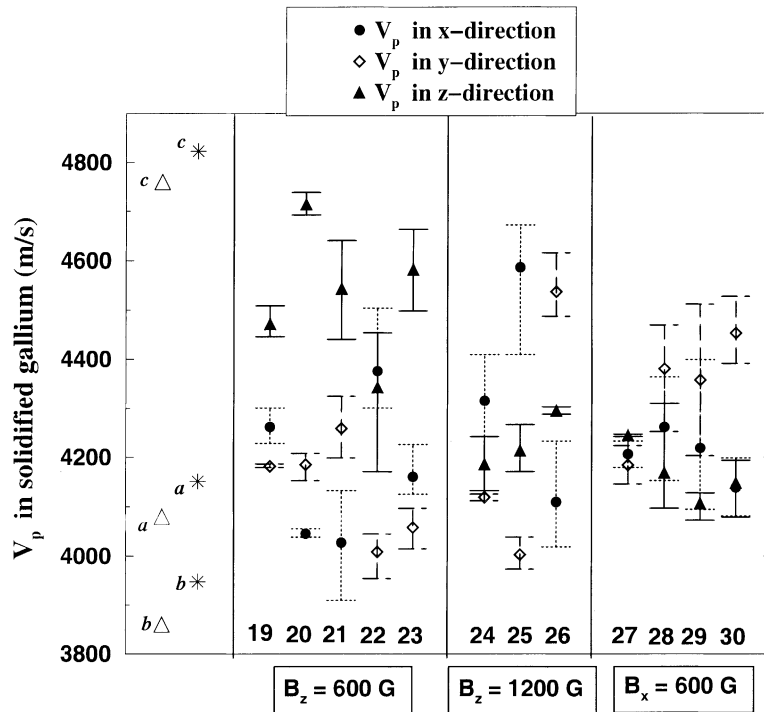
Fig. 11. Ultrasonic measurements of V_P in gallium solidified in a vertical temperature gradient and a uniform magnetic field (either horizontal B_x or vertical B_z), from experiments 19–30 (see Table 3). V is measured at six locations along the x-and y-directions and at four locations along the z-direction. Data points are the average of the locations and error bars represent the deviation around the average between the minimum and the maximum measured values. The values of V_P along the three symmetry axes of single crystal Ga$_\alpha$ are plotted for reference (see Table 1). Measurement errors are typically 50 m/s.

of anisotropy as obtained in the experiments with a vertical temperature gradient (Fig. 9).

Fig. 11 summarizes the results of directional crystallization in the presence of different imposed magnetic fields, subject to a variety of different thermal gradients (see Table 3). In this set of experiments, the magnetic field strength is either 60 or 120 mT. The corresponding Hartmann numbers (see Table 2) are 200 and 400, respectively, indicating that the Lorentz force far exceeds the viscous force in the melt. We find that the amount of anisotropy and the variety of principal directions in these experiments are about the same as the cases without an imposed magnetic field, as can be seen by comparison with the results shown in Figs. 9 and 10. We also note that the direction of anisotropy from solidification in an imposed magnetic field varies from one experiment to the next. As with the non-magnetic experiments, we do not see a tendency for one particular crystallographic axis to orient with the

imposed magnetic field direction. We conclude that the Lorentz force from the magnetic field is not a controlling factor in the primary crystallization, and does not impose a preferred axis of growth.

Our overall conclusion from the three sets of experimental results in Figs. 9–11 is high degrees of anisotropy are the rule in directional solidification of gallium. About one half of the experiments result in polycrystalline anisotropy in excess of 50% of the anisotropy for a single crystal of gallium. Conversely, only rarely did we obtain an isotropic solid (only one experiment out of 30, experiment 27 of Fig. 11). Significantly, we did not detect any systematic influence on the orientation of the anisotropy from an imposed magnetic field.

In Fig. 12, we summarize the results of experiments where the solidification was nearly isotropic, rather than directional. In these experiments, we applied the same (uniform) temperature to all sides of the
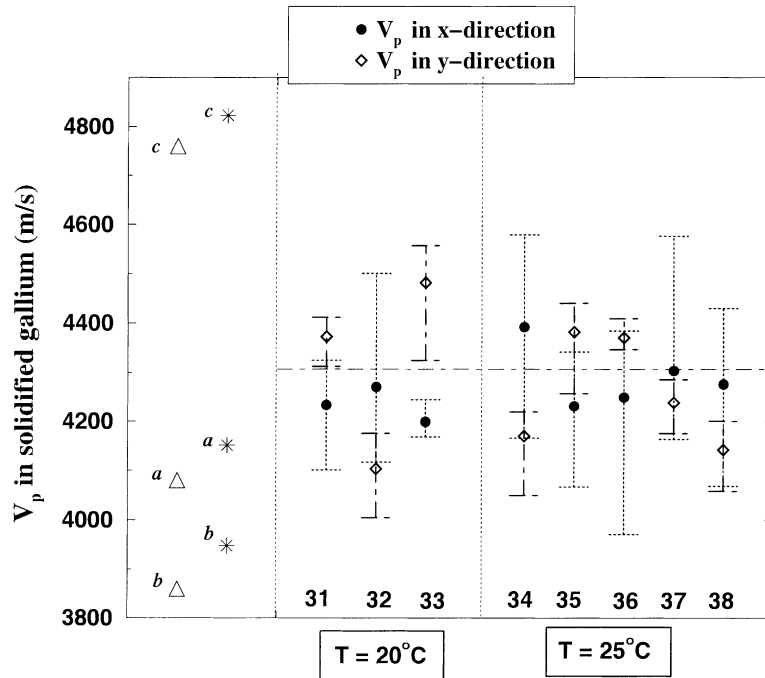
Fig. 12. Ultrasonic measurements of V_P in gallium solidified in a radial temperature gradient, from experiments 31–38 (see Table 3). In these experiments, V_P is only measured at six locations along the *x*- and *y*-directions. Data points are the average of the locations and error bars represent the deviation around the average between the minimum and the maximum measured values. The values of along the three symmetry axes of single crystal Ga$_\alpha$ are plotted for reference (see Table 1). Measurement errors are typically 50 m/s.

chamber, so that the melt solidified inward from each surface at approximately the same rate. Because of the additional boundary temperature control, we were not able to obtain velocity measurements in the *z*-direction for these cases.

In general, the solid resulting from these experiments is more isotropic than in the experiments with a unidirectional temperature gradient. Evidently, when solidification occurs simultaneously on all six faces there is more randomization of crystallographic axis orientation, compared to directional solidification along a single planar front. Even so, we find substantial spatial variation in wave speeds, as shown in Fig. 12. Our conclusion from this set of experiments is that isotropic solidification results in a smaller amounts of anisotropy compared to unidirectional solidification, but it also results in greater textural heterogeneity.

In another set of experiments, we examined the possible influence of solid grains remaining in the melt

from one experiment to the next, the type-2 initial condition described previously. The residual solid material remaining after re-melting consisted mostly of gallium oxides, formed from interaction with the atmosphere. The density of the oxides is less than pure gallium, so some of the solid residue floats to the top of the chamber, while some of it adheres to the side walls, creating initial nucleation sites with a preferred crystallographic orientation.

Fig. 13 shows results from a sequence of type-2 experiments. In this sequence, besides the experimental conditions shown before (Figs. 9–11), a new type of fluid flow is tested: a small propeller generates a swirling flow in the melt. This turbulent swirling flow (see Table 2) includes differential rotation and might be a good analogue of the flow taking place in the neighborhood of the inner core, if super rotation of the inner core occurs or if the flow of the liquid flow includes a strong toroidal component. The remarkable result in this sequence (Fig. 13) is that beginning with
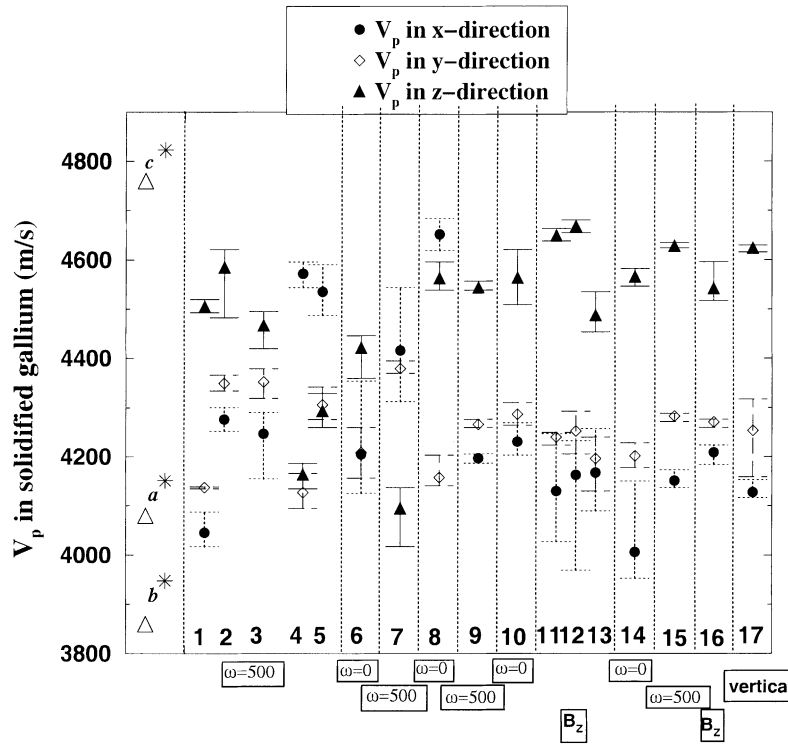
Fig. 13. Ultrasonic measurements of V_P in gallium solidified under different external controls, from experiments 1–17 (see Table 4): ω denotes turbulent mixing generated by a small propeller rotating at 500 rev/min in the liquid, B_z denotes an imposed vertical magnetic field. All the experiments are done in a horizontal temperature gradient except experiment 17 made in a vertical temperature gradient. V_P is measured at six locations along the x- and y-directions and at four locations along the z-direction. Data points are the average of the locations and error bars represent the deviation around the average between the minimum and the maximum measured values. The values of V_P along the three symmetry axes of single crystal Ga_α are plotted for reference (see Table 1). Measurement errors are typically 50 m/s.

experiment 9, the anisotropy is unchanged, regardless of which of the following external controls are applied: turbulent mixing of the melt, natural convection in the melt, magnetic fields, or directional solidification driven by either vertical cooling or horizontal temperature gradients. It is within sequences such as these that we obtain reproducible results from one experiment to the next. However, this reproducibility is not just the result of external controls. Instead it mostly reflects an internal control: the same residual solid grain serves as initial nucleation sites from one experiment to the next.

In order to better delineate the true anisotropy, we compute ensemble average velocities from multiple experiments made under similar conditions. The resulting ensemble averages are shown in Fig. 14. Six

ensemble averages are shown. Set 1 is the average of all nine experiments in Fig. 9 with a conductive (stable) vertical thermal gradient; set 2 is the average of all experiments in Fig. 10 with a horizontal thermal gradient; set 3 is the ensemble average of all experiments in Fig. 11 with an imposed magnetic field; set 4 is the average of all experiments in Fig. 12 with radial thermal gradients; set 5 is the ensemble average of all 17 type-2 experiments (without cleaning) from Fig. 13; set 6 is the ensemble average of experiments 9–17 in Fig. 13, without cleaning, the sequence of experiments which gave the most reproducible results.

The ensemble averages in Fig. 14 that show strong anisotropy are from the type-2 experiments. This result again demonstrates our main finding, that the lattice preferred orientation (LPO) of the solid is mostly
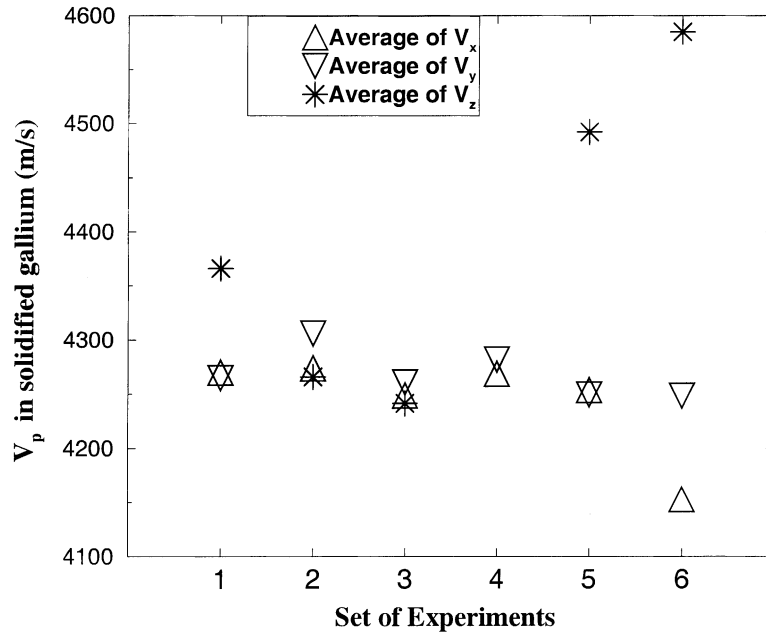
Fig. 14. Ensemble average directional ultrasound velocities in solid gallium from multiple experiments with similar external conditions. Velocities in the x-, y-, z-directions are shown. Set 1 is the average of all experiments in Fig. 9 with a conductive (stable) vertical thermal gradient; set 2 is the average of all experiments in Fig. 10 with a horizontal thermal gradient; set 3 is the ensemble average of all experiments in Fig. 11 with an imposed magnetic field; set 4 is the average of all experiments in Fig. 12 with radial thermal gradients; set 5 is the ensemble average of all 17 type-2 experiments from Fig. 13; set 6 is the ensemble average of experiments 9–17 from Fig. 13.

controlled by presence of seed grains present in the initial melt. However, Fig. 14 also reveals a weak tendency for the ultrasonically fast direction of the solid to align with the vertical, a result not evident in the data from individual experiments. Ensemble averages of experiment sets 1, 5, and 6 in Fig. 14 all show ultrasonically fast propagation in the vertical direction. For sets 5 and 6, fast vertical propagation may be just an artefact of the initial grain orientations, since these were all type-2 experiments. But the fast vertical propagation in set 1 cannot be explained this way, since these were type-1 experiments. We infer then, that the vertical directional solidification in experiment set 1 produces an average textural orientation and about 2% transverse elastic anisotropy. Vertically oriented transverse anisotropy can be produced by a statistical vertical alignment of the ultrasonically fast c-axis, and is consistent with preferred growth along that axis in the vertical thermal gradient. The nearly uniform directional velocities in experiment set 2

suggests the effect of a horizontal thermal gradient on texture development is not as strong as the vertical thermal gradient in set 1. Likewise, the uniform directional velocities in set 3 indicate the magnetic field orientation has little control on the solidification texture.

5. Summary

All of our experiments resulted in polycrystalline solid gallium with crystal elongation parallel to the imposed thermal gradient. In almost every case (only one exception out of 55 experiments) we measured spatially coherent compressional wave anisotropy, ranging from 20–80% of single crystal values for gallium. We found that the elastic velocity is spatially heterogeneous, with compressional wave speed variations detected over individual faces of the solid. This spatial variation may be grain size dependent, since each individual ultrasound ray path sampled

only a small number of grains. Perhaps most surprisingly, we find that the growth direction does not always coincide with the direction of any particular crystallographic axis, nor does it necessarily coincide with the bulk symmetry axis of the polycrystal as defined by the orientation of the compressional wave anisotropy.

We examined the influence of external environmental controls on solidification, including vertical and horizontal thermal gradients (with and without free convection), turbulence in the melt, imposed magnetic field, rotation, and isotropic cooling. We find that directional cooling produces more anisotropy and more crystal elongation compared to isotropic cooling. In type-1 experiments, where the initial condition is melt free from nucleation grains, the resulting anisotropy is not sensitive to external controls such as magnetic fields, rotation, and imposed motions in the melt. However, we do find a statistical tendency for the ultrasonically fast direction to align with the vertical in experiments with vertical thermal gradients and vertical directional solidification. This relationship is similar to the findings of Bergman (1997) and Bergman et al. (2000). It is consistent with vertical transverse anisotropy, that is, statistical alignment of the ultrasonically fast *c*-axis parallel to the vertical, and random alignment of the other symmetry axes in the horizontal plane. In type-2 experiments, where the initial condition is in situ melting of the previous experiment, the resulting anisotropy was large and was often repeatable in terms of both direction and magnitude.

We have tracked the propagation of the solidification front using ultrasonic measurements. In type-1 experiments the front advances as the square root of time, in accord with theory for a solidifying liquid half space. Using temperature measurements, we identify several stages of directional solidification, including supercooling of the melt, the temperature for initial nucleation, the solidification phase with latent heat release, and the final cooling phase of the solid.

Taken together, these findings indicate that the LPO in our directionally solidified gallium is influenced by the thermal gradient, which determines the crystal growth direction, but not measurably influenced by the other external environmental factors we considered. The LPO of our single component metal solid is primarily controlled by presence of seed grains present in the initial melt, and secondarily by vertical thermal gradients.

6. Implications for the inner core

Because the chemistry of the core is uncertain and because it is impossible to reproduce the physical environment of the ICB region, results from solidification experiments cannot be applied directly to the inner core. In addition, our results are derived from crystallization from a single component melt, and the results may differ in a multicomponent melt like the outer core. However, solidification experiments in simple liquid metal compounds can provide some insight into basic mechanisms that might affect the way the inner core crystallizes.

In this study, we have found two factors that exert measurable control on development of elastic anisotropy in directionally solidified gallium. These are (1) the direction of the basic state temperature gradient and (2) the presence or absence of nucleation grains on which the solid phase first grows. The important role of pre-existing texture, together with the insensitivity we have found to external environmental factors (other than temperature gradient), suggests a new interpretation of the seismic anisotropy observed in the inner core. According to our results (consistent with previous solidification experiments; see Bergman et al., 2000), the inner core grows by crystallization at the ICB with grain elongation mostly in the radial direction, the direction of the local conductive heat flow vector. The rate of crystallization is proportional to the magnitude of the local conductive heat flow vector, and need not be uniform over the ICB. It may be greatest near the inner core equator for example, as proposed by Yoshida et al. (1996). However, the seismic anisotropy of the newly-formed solid does not reflect just the radial growth direction alone. Instead, our results suggest that the texture of the newly formed solid at each location on the ICB results from a combination of the local thermal environment plus the texture of the solid already formed there. This style of crystallization favors the development of a solid consisting of large-scale, anisotropic regions, in which the directions of the symmetry axes of the anisotropy may vary from one domain to the next and provides a

simple explanation for heterogeneities in inner core anisotropy.

Acknowledgements

References

Bergman, M.I., 1997. Measurements of elastic anisotropy due to solidification texturing and the implications for the Earth's inner core. Nature 389, 60–63.

Bergman, M.I., Giersch, L., Hinczewski, M., Izzo, V., 2000. Elastic and attenuation anisotropy in directionally solidified (hcp) zinc, and the seismic anisotropy in the Earth's inner core, and the seismic anisotropy in the Earth's inner core. Phys. Earth Planet. Int. 117, 139–151.

Beyer, R.T., Ring, E.M., 1972. In: Beer, S.Z. (Ed.), Liquid Metals: Chemistry and Physics. Marcel Dekker, New York (Chapter 9).

Brito, D., Nataf, H.-C., Cardin, P., Aubert, J., Masson, J.-P., 2001. Ultrasonic doppler velocimetry in liquid gallium. Exp. Fluids. 31 (6), 653–663.

Creager, K.C., 1997. Inner core rotation from small-scale heterogeneity and time varying travel times. Science 278, 1284–1288.

Creager, K.C., 1999. Large-scale variations in inner core anisotropy. J. Geophys. Res. 104, 23137–23139.

Cubbery, W.H., 1979. Metal Handbook II, 9th Edition. American Society of Metals, Metals Park, OH, pp. 736–737.

Curien, H., Rimsky, A., Defrain, A., 1961. Atomic structure of a crystalling phase of gallium unstable at atmospheric pressure. Bull. Soc. France Min. Crist. 84, 260.

Jeanloz, R., Wenk, H.R., 1988. Convection and anisotropy of the inner core. Geophys. Res. Lett. 15, 72–75.

Karato, S., 1993. Inner core anisotropy due to the magnetic field-preferred orientation of iron. Science 262, 1708–1711.

Karato, S., 1999. Seismic anisotropy of the Earth's inner core resulting from flow induced by Maxwell stresses. Nature 402, 871–873.

Laske, G., Masters, G., 1999. Limits on differential rotation of the inner core from an analysis of the Earth's free oscillations. Nature 402, 66–69.

Lide, D.R., 1995. Handbook of Chemistry and Physics, 75th Edition. CRC Edition.

Lyall, K.R., Cochran, J.F., 1971. Velocity of sound and acoustic attenuation in pure gallium single crystals. Can. J. Phys. 49, 1075–1097.

McSweeney, T.J., Creager, K.C., Merrill, R.T., 1997. Depth extent of inner core seismic anisotropy and implications for geomagnetisin. Phys. Earth Planet. Int. 101, 131–156.

Morelli, A., Dziewonski, A.M., Woodlionse, J.H., 1986. Anisotropy of the inner core inferred from PKIKP travel times. Geophys. Res. Lett. 13, 1545–1548.

Nicolas, A., Poirier, J.-P., 1976. Crystalline Plasticity and Solid State Flow in Metamorphic Rocks. A Wiley/Interscience Publication, Wiley.

Nondestructive Testing Handbook, 1991. Ultrasonic Testing ASNT, Vol. 7, 2nd Edition. Paul McIntire.

Okada, K., Ozoe, H., 1992. Transient responses of natural convection heat transfer with liquid gallium under an external magnetic field in either the *x*-, *y*-, or *z*-direction. Ind. Eng. Chem. Res. 31, 700–706.

Poupinet, G., Pillet, R., Souriau, A., 1983. Possible heterogeneity of the Earth's core deduced from PKIKP travel times. Nature 304, 204–206.

Reed-Hill, R.E., 1973. Physical Metallurgy Principles, Second Edition. PWS-KENT Publishing company, Boston, pp. 568–610.

Roughton, N.A., Nash, H.C., 1962. Single Crystal Elastic Constants of Gallium. Office of Naval Research, Technical Report, No. 6.

Sabot, J.-L., Lauvray, H., 1995. Gallium and Gallium Compounds in Kirk-Othmer, Encyclopedia of Chemical Technology, Vol. 12, 4th Edition. pp. 299–317.

Song, X., 1997. Anisotropy of the Earth's inner core. Rev. Geophys. 35, 297–313.

Song, X., Richards, P.G., 1996. Observational evidence for differential rotation of the Earth's inner core. Nature 382, 221–224.

Song, X., Helmberger, D.V., 1998. Seismic evidence for an inner core transition zone. Science 282, 924–927.

Souriau, A., Poupinet, G., 2000. Inner core rotation: a test at the world-wide scale. Phys. Earth Planet. Int. 118, 13–27.

Spells, K.E., 1936. The determination of the viscosity of liquid gallium over an extended range of temperature. Proc. Phys. Soc. 48, 299–311.

Stixrude, L., Cohen, R.E., 1995. High pressure elasticity of iron and anisotropy of Earth's inner core. Science 267, 1972–1975.

Stixrude, L., Wasserman, E., Cohen, R.E., 1997. Composition and temperature of Earth's inner core. J. Geophys. Res. 102, 24729–24739.

Subramanian, P.R., Laughlin, D.E., 1990. In: Massalski, T.B., Okamoto, H., Subramanian, P.R., Kacprzak, L. (Eds.), Binary Alloy Phase Diagrams. ASM International, Materials Park.

Sumita, I., Olson, P.L., 1999. A laboratory model for convection in Earth's core driven by a thermally heterogeneous mantle. Science 286, 1547–1549.

Sumita, I., Yoshida, S., Kumazawa, M., Hamano, Y., 1996. A model for sedimentary compaction of a viscous medium and its application to inner core growth. Geophys. J. Int. 124, 502–524.

Tanaka, S., Hamaguchi, H., 1997. Degree one heterogeneity and hemispherical variation of anisotropy in the inner core from PKP(BC)-PKP(DF) times. J. Geophys. Res. 102, 2925–2938.

Turcotte, D.L., Schubert, G., 1982. Geodynamics. Applications of Continuum Physics to Geological Problems. Wiley, New York, p. 450.

Vidale, J.E., Earle, P.S., 2000. Fine-scale heterogeneity in the Earth's inner core. Nature 404, 273–275.

Weeks, W.F., Gow, A.J., 1978. Preferred crystal orientations in the fast ice along the margins of the Atlantic Ocean. J. Geophys. Res. 83, 5105–5121.

Yoshida, S., Sumita, I., Kumazawa, M., 1996. Growth-model of the inner core coupled with the outer core dynamics and the resulting elastic anisotropy. J. Geophys. Res. 101, 28085–28103.